Role of Computational Parameters on Predicting Self-Consistent Residual Stress and Distortion during Wire Arc Additive Manufacturing

Examining the effects of mesh- and time-step resolutions during transient finite element analysis of a large-scale (248 layers) metallic part

BY B. SOLSBEE, Y. LEE, S. SIMUNOVIC, AND S. S. BABU

Abstract

Production of three-dimensional metallic parts through integration of an articulated robot and gas metal arc welding, also known as wire arc additive manufacturing (WAAM), can produce large-scale components with moderate geometrical complexity. This technology is particularly appealing due to its high deposition rates, scalability, and cost-effective feedstock compared to other AM processes. Despite its advantages, WAAM adoption is hindered by challenges in ensuring geometric conformity without extensive distortion, defect-free structures, and consistent mechanical properties. Finite element analysis (FEA) is often used to address the challenge of geometrical conformity. As the size of parts increases, the best practices for mesh size and temporal resolution known in the literature become computationally unviable. This research examined the effects of mesh and time-step resolutions during transient FEA of a large-scale (248 layers) metallic part. The impact of computational parameters on the thermal history, displacement, and residual stress distributions were evaluated. The results showed that predicted distortion was consistent across resolutions, while time-step length significantly affected predicted thermal history, and mesh size influenced residual stress distributions. To investigate this relationship further, directionally biased meshes were considered and analyzed. The results indicated that increasing mesh resolution perpendicular to the welding path yielded stress predictions that aligned closely with higher-resolution models while offering substantial computational savings. The significances of this research are related to verification and validation of WAAM models for widespread industrial adoption and pragmatic guidelines for optimizing computation parameters for balancing computational efficiency and predictive accuracy of residual stress and distortion.

Keywords

- Wire-Arc Additive Manufacturing
- Large-Scale Part
- Finite Element Analysis
- Distortion
- Residual Stress
- Verification and Validation

Introduction

Metal additive manufacturing (AM), which integrates robotics and gas metal arc welding technology, also known as wire arc additive manufacturing (WAAM) or wire arc direct energy deposition (wire-arc DED), is considered an ideal process for making large-scale components with simple to moderate geometric complexity. The shift to WAAM from traditional manufacturing is motivated by the decrease in domestic casting facilities, which have declined from 6150 in 1955 to 1770 in 2022 (Ref. 1). The U.S. Department of Defense has identified the casting and forging industry supply chain and recent labor and component shortages as a critical threat (Ref. 2). The WAAM process (Refs. 3, 4) presents its own advantages, including high deposition rate, high scalability (Ref. 5), less expensive wire (Ref. 6), and the ability to combine one or more robotic systems (Refs. 7, 8) in parallel to other powder bed fusion (PBF) processes. Specifically, it can

https://doi.org/10.29391/2026.105.001

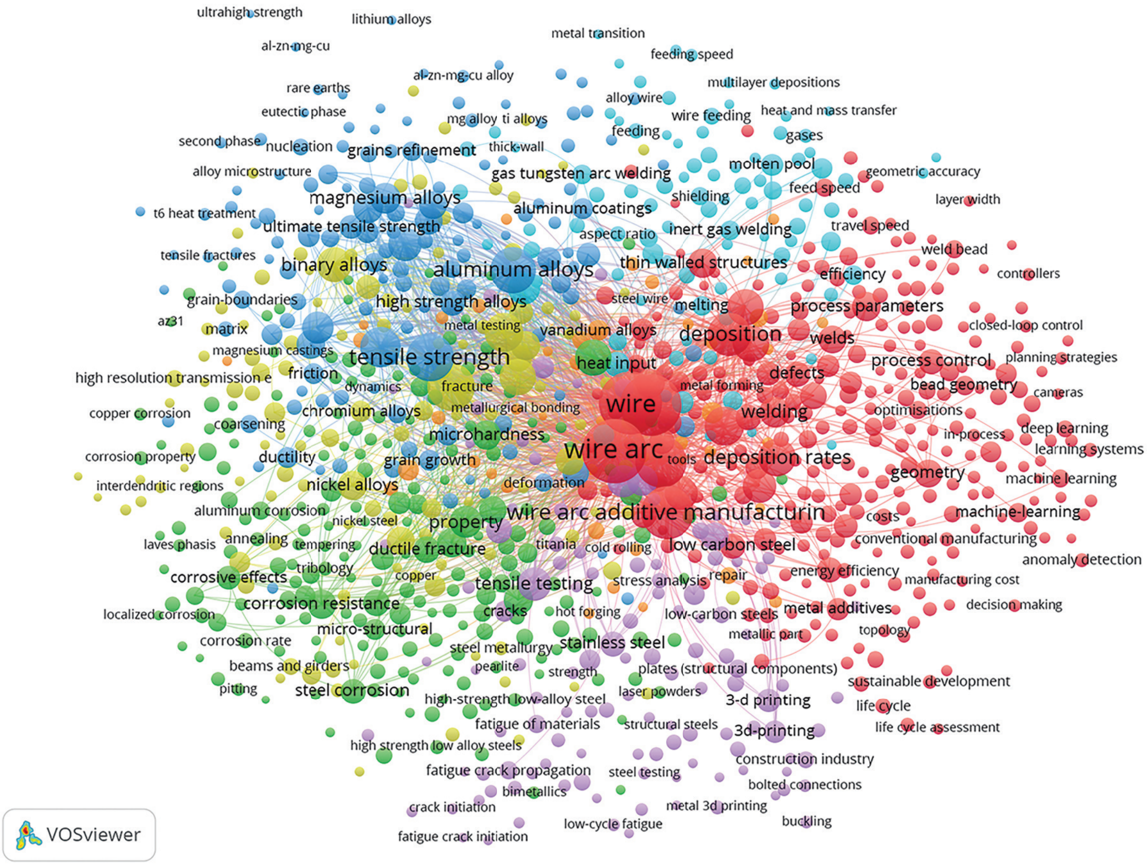

Fig. 1 — Network analysis based on subject index in 4000-plus publications related to wire arc additive manufacturing. The current paper corresponds to the prediction of geometrical conformity (i.e., distortion) and the residual stresses.

deposit material at rates of up to 10 kg/h in steel, while laser wire processes can reach up to 3 kg/h, and powder-based processes can approach a maximum of 6 kg/h (Refs. 9, 10). Regarding the materials feedstock, the price of stainless-steel wire can vary between $3/kg and $18/kg, while the cost of stainless-steel powder ranges from $78/kg to $120/kg (Ref. 11). Consequently, the WAAM process, when combined with post-process machining, can be relatively accessible for even small- and medium-scale industries. However, widespread adoption of WAAM faces three major challenges: (1.) ensuring defect-free (or minimal defects) and a reproducible microstructure throughout the entire component; (2.) achieving consistent mechanical properties in the deposited part while also developing a method to confirm the performance of the final part; (3.) ensuring that the part's geometry conforms to the desired design (Ref. 12). A network analysis of 4000-plus articles in Fig. 1 shows that researchers have focused on various aspects of the above three challenges from different perspectives in the last ten years. Although extensive scientific and technical efforts (Refs. 13–16) exist with respect to WAAM on microstructure, properties, automation, and filler wire development, this research is specifically dedicated to addressing the third challenge: geometrical conformity. Specifically, we address the following question: Is it possible to calculate the consistent residual stress and distortion distributions within a large WAAM part without a large computational penalty with available finite element models?

Similar to other additive manufacturing or welding processes, localized deposition of molten material during WAAM results in transient and nonuniform thermal gradients. These thermal gradients lead to complex triaxial thermal stresses within the part, which are combined with their external mechanical constraints (e.g., clamping) and inherent constraints due to the evolving part geometry. Consequently, these thermal stresses lead to nonuniform plastic deformation in the part, which changes the trajectory of the geometry being built. Finally, on cooling, due to the presence of accumulated plastic strain gradients, a complex distribution of locked-in elastic residual stresses is induced within the parts. Interestingly, these residual stress distributions and part distortions are highly sensitive to post-process operations such as machining, hammering, and heat treatment. The legacy knowledge on residual stress and distortion exists in the literature, and readers are referred to the same for more information (Refs. 17, 18).

The primary goal of AM is to produce a near-net shape of the final component without post-processing. However, extensive part distortions may necessitate overbuilding and excessive post-process machining to achieve the net shape. If the final part cannot be placed within the envelope of the

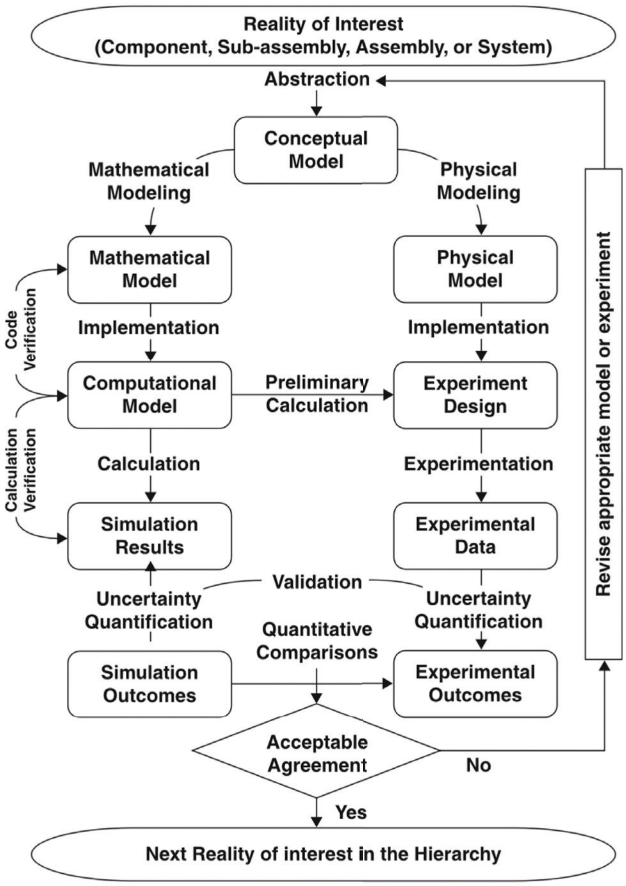

Fig. 2 — Schematic illustration of verification and validation process flow for computation weld mechanics (Ref. 28).

final print geometry, the whole printed part may have to be rejected for noncompliance with the intended CAD geometry. Consequently, these challenges mandate expensive trial-and-error experimental optimization to arrive at a final shape. Since manufacturing time for a large-scale WAAM part may range from days to months, the above challenges may make the WAAM not viable for industrial adaptation. Therefore, there is a need to produce parts that are as close to the desired geometry as possible, or near net shape, to justify the technical and business case for adoption of AM. One of the pathways to overcoming the extensive trial and error challenge in the WAAM process is to leverage computational models developed for welding (Refs. 19, 20). This computational approach should be able to predict consistent residual stresses and distortions during the process design stage, thereby allowing operators to adjust manufacturing inputs such as welding sequence, input power, and even the geometry itself, to arrive at desirable outcomes (Refs. 21–23).

Any approach based on computational model-based iterations to optimize process development should be faster than the time needed for experimental iterations. One of the rapid modeling schemas for distortion prediction is based on the inherent strain method outlined in the article by Tsai and Kim (Ref. 24). This approach uses a purely mechanical finite element analysis (FEA) by applying plastic strains to a geometry as elements are activated along the planned welding path or layer-wise. Depending on the physics considered, inherent strain FEA has the potential to generate extremely fast linear solutions, which enables the iteration of pre-deformed geometry. However, it can be difficult to relate the applied strains as a function of welding process parameters, particularly under varying local mechanical constraints and dynamic changes to the overall geometry of the WAAM build. One of the most prevalent approaches to predict residual stress and distortion in welding and the WAAM process is a sequentially coupled thermomechanical (TM) FEA, which was originally developed by welding researchers (Ref. 18) and has been adopted by AM researchers (Ref. 25) and commercial software vendors (Refs. 26, 27) worldwide. In this method, thermal histories are calculated a priori over a part's domain and applied as transient loading conditionsfor elastic-plastic mechanics calculations are performed to estimate the evolving elastic and plastic strain distributions. Depending on model fidelity and the physics considered, computational costs can rapidly increase, a problem further exacerbated as analysis expands to larger parts. To facilitate the adoption of computational weld mechanics in the industry, the American Welding Society (AWS) developed a guide for verification and validation (V&V) methodologies (see Fig. 2) (Ref. 28). This paper pertains to our first attempt at the V&V of computational tools for predicting the residual stress and distortion in large-scale WAAM parts.

It is common practice during finite element analysis of WAAM components to use an element size less than or equal to the width and height of the deposition cross-section to accurately represent the physical response to metal deposition (Refs. 21–23, 25). The selection of element size in an FEA model should be based on mesh-convergence analysis, where a representative domain is used to find an acceptable balance of error and computational time. In the case of WAAM, the representative geometry consists of several beads or layers. For example, when modeling WAAM deposition of aluminum ally 5183, Zhao et al. (Ref. 21) conducted a mesh convergence study using mesh sizes of one, two, and three elements across the height and width of the deposition cross-section by analyzing ~2.25 beads from the full part. Based on the study, the 2 × 2 element approach was justified by its 0.49% relative error while arriving at a solution 61.4 h faster. Nevertheless, due to the challenges associated with computational costs, it is uncommon to report the impact of mesh size on the results of full WAAM geometries at larger, more practical dimensions in open publications. One example is seen in Yang et al. (Ref. 29), wherein a computationally efficient semi-analytical thermal model analysis was coupled with a mechanical analysis to model the deposition of a four-layer thin-wall structure. When investigating the thermal results, it was found that a finer mesh (5 mm × 0.3125 mm × 2 mm) yielded nearly identical temperature history as a coarser mesh (5 mm × 1.25 mm × 2 mm), which was then used in the mechanical analysis. However, the impact of different resolutions on the self-consistency of distortion and residual stress distribution was not attempted. Further investigations of resolution can be seen in the modeling of other AM processes. Cattenone et al. (Ref. 30) investigated the effects of temporal and spatial resolution on the results of a complete part geometry in TM analysis of fused deposition

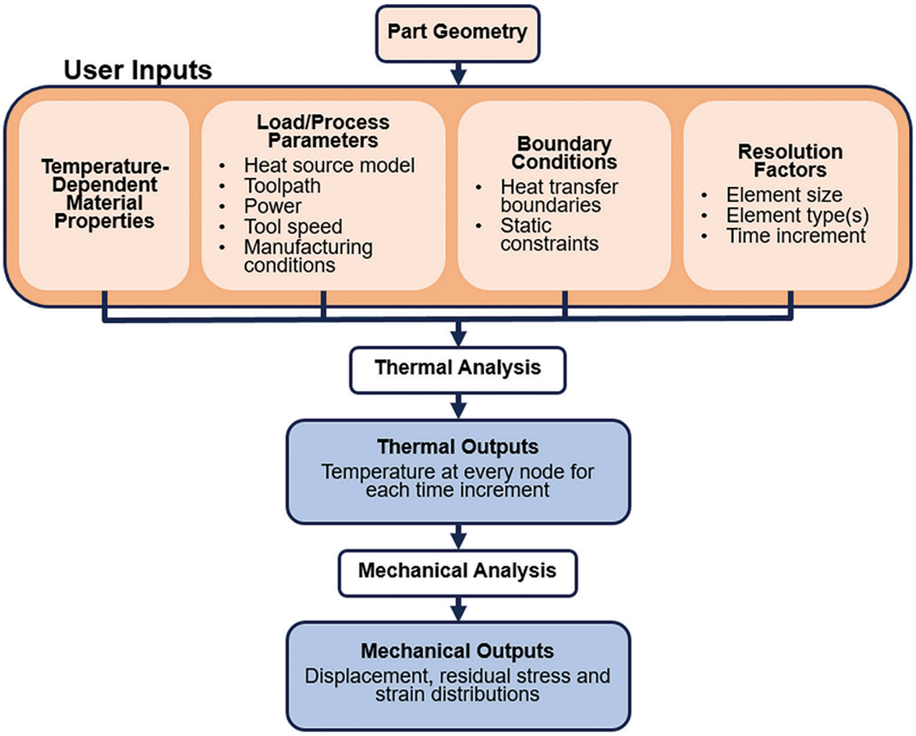

Fig. 3 — Computational workflow for sequentially coupled thermo-mechanical finite element analysis used in this research. The approach was implemented within a commercial software.

Table 1 — Finite Element Method Parameters Explored in the Current Research as a Part of the Verification and Validation

Simulation Number	Element Size, ℓ (mm)	Time Increment, Δt (s)	Total Elements in Part	Fourier Number (F_o)	Total Solution Time (h)
1	8	400	8184	22.6223	0.33
2	8	100	8184	5.65556	0.81
3	8	25	8184	1.41389	1.89
4	4	400	64,976	90.4890	2.35
5	2	400	587,016	361.956	49.97

modeling of thermoplastics, implementing elements ranging from 50% of the bead width and height to 4× the bead width while maintaining a z height of the elements consistent with deposited layer height. The authors reported that the time step greatly influenced local temperature development while having a minimal impact on mechanical results. A coarser meshing strategy can fail to capture local stress concentrations, demonstrating a need to further explore the impact of resolution on complete parts. Lu et al. (Ref. 31) implemented a four-layer activation scheme in modeling powder-based directed energy deposition (DED) of Ti-6Al-4V to speed up TM FEA calculations. By adjusting the time step, the calculations were forced to activate four layers in a single step. From the simulations, it was observed that a larger time step generated excessive oscillations in the temperature history, while the average temperature values were in line with measured data. Due to the inability to fully capture thermal gradients across the substrate in the first four-layer group in the early transient stages, a mismatch of displacements (i.e., difference between experimental and modeled distortion) greater than 1 mm was observed. However, as the process approached a steady state, the results from numerical analysis were in good agreement with measured displacements. Overall, this approach was able to reduce computation time by 77%. Nycz et al. (Ref. 32) explored the relationship between time increment size and residual stress predictions in mild steel wall geometry

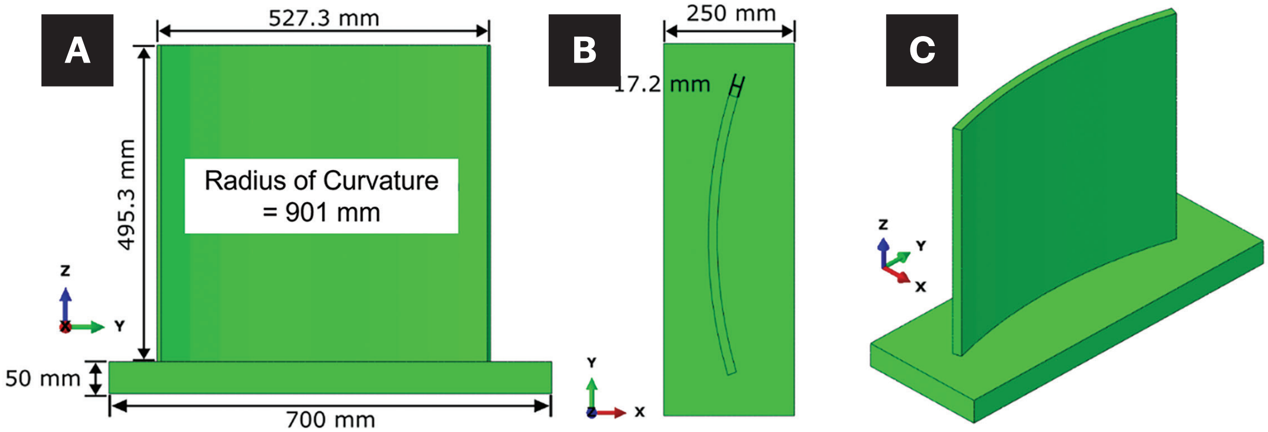

Fig. 4 — Schematic illustration of the part geometry: A — Front view on the YZ plane; B — top view on the XY plane; C — isometric view.

Table 2 — Predicted Maximum Temperatures at Various Increment Sizes and Element Sizes

Increment Size	400 s	100 s	25 s
Maximum Temperature (°C)	698.4	784.5	971.6
% Difference	—	12.3%	39.1%
Element Size	8 mm	4 mm	2 mm
Maximum Temperature (°C)	698.4	683.3	682.8
% Difference	—	≈ 2.2%	≈ 2.3%

manufacturing using WAAM, where each layer consisted of two tracks of continuously deposited material. A 20-s time increment captured substrate distortion and showed consistent residual stresses with a 10-s time increment. However, neutron diffraction measurements revealed tensile longitudinal residual stresses near the surface of the substrate that weren't captured by the larger increment sizes. To remedy this, an increment size of 1 s was used for the first three layers, followed by 20 s for the remaining layers to better capture the stress accumulation caused by interaction between the initial layers and the substrate while maintaining computational efficiency. Deering et al. (Ref. 33) investigated the impact of various user inputs on the results of TM FEA of powder bed fusion of stainless steel 316, including increment and mesh resolution. The findings indicated that average temperature increases with higher resolution in both increment size and mesh; however, the study reported a range of only 2.33°C. Additionally, it was observed that larger elements predicted higher residual stresses, and both larger elements and increment size resulted in less displacement. The work concluded that the impact of mesh density and increment size are independent, and an increment size encapsulating two to four physical layers was recommended to balance accuracy and runtime when modeling the PBF process. Although the critical need to understand the sensitivity of modeling parameters on residual stress and distortion prediction were stressed by the AWS and ANSI guides for verification and validation in computational weld mechanics had been published (Ref. 28), to our disappointment, the computational modeling literature with reference to large-scale WAAM appears to be ignoring this critical aspect (Ref. 34). We believe that this prevailing attitude in the community is partly due to the pressures to make predictions of distortion with minimal computing costs, as well as to arrive at computational optimizations that are faster and completed at a relatively small fraction of the time required for experiential optimization.

Based on a review of the literature, this paper aims to investigate how computational mesh size and time resolution factors affect the prediction of distortion and residual stresses in the WAAM process at a practical scale. This work is a continuation of the findings and modeling from Lee et al. (Ref. 35), which investigated the mode of deformation for a large-scale (≈500 mm tall and wide), curved wall geometry. The work focused on variable printing stops due to manufacturing conditions using sequentially coupled TM FEA. The modeling results were compared with laser scanning measurements and DIC analysis. Ultimately, this paper aims to provide practical guidelines for simplifications that reduce computational cost while still accurately predicting geometric deformation, making the approach suitable for industrial adoption.

Computational and Experimental Details

A series of finite element analyses for producing a curved wall (Ref. 35) geometry using the WAAM process were performed in this research. The analyses considered various element sizes and time increment steps. Abaqus Standard 2022 software was used with the AM Modeler plug-in to conduct the study. From the analyses, nodal displacement, residual stresses, and thermal history were extracted and compared between each run. Additionally, the deformed analysis output geometries were compared to a point cloud of the physical geometry manufactured by WAAM using optical measurements.

Computational Modeling Details

An overview of the TM analysis procedures used in this simulation is schematically outlined in Fig. 3 (Refs. 18, 32, 36). The temperature-dependent thermomechanical properties of SS316L from the literature (Refs. 35, 37, 38) were assigned for the parts. All simulations were generated on 12 cores of an Intel Xeon CPU E5-26300 processor. The tool path was converted from machine G-code into the Abaqus event series file using an in-house Perl script. The data included x, y, and z coordinates, arc-power, and time stamps over the history of the manufacturing process. The event series was used to prescribe the motion of the heat source and material deposition via progressive element activation. To fully capture the manufacturing process, this series included pauses for machine maintenance and adjustments such as tip change, wire changes, and print stop (Ref. 35), which were not known prior to deposition. The widely accepted Goldak's double ellipsoid heat source (Ref. 36) was used in this work; however, it often does not need to be considered at this scale because cuboid or concentrated heat sources have been shown to produce sufficiently good prediction of thermal signatures (Refs. 21, 32). Progressive element activation was implemented for the analyses, which updated the domain for each increment by activating elements along the tool path to simulate material deposition. Prior to activation, elements do not participate in the analysis solution. As elements were activated, the thermal boundary conditions for heat loss by convection and radiation were automatically updated to account for the change in free surface of the deposited volume. For further details on the progressive element activation method, the reader is referred to the previous work (Ref. 35).

WAAM Experimental Information

The simulated part geometry, shown in Fig. 4, consisted of 248 layers, each with an approximate height of 2 mm. The total part height was 495.3 mm and took 11 h to manufacture (including cool down) using a standard WAAM robotic cell. Each layer consisted of two contour passes creating four beads (two inner beads and two outer beads), alternating between the scan pattern shown in Fig. 5A for odd layers and Fig. 5B for even layers, at a speed of 16.93 mm/s. The substrate consisted of AISI 1080 steel, and the WAAM part material was 316L stainless steel. Arc power was 5.83 kW, and a mixture of 98% Ar and 2% CO2 was used as a shielding gas.

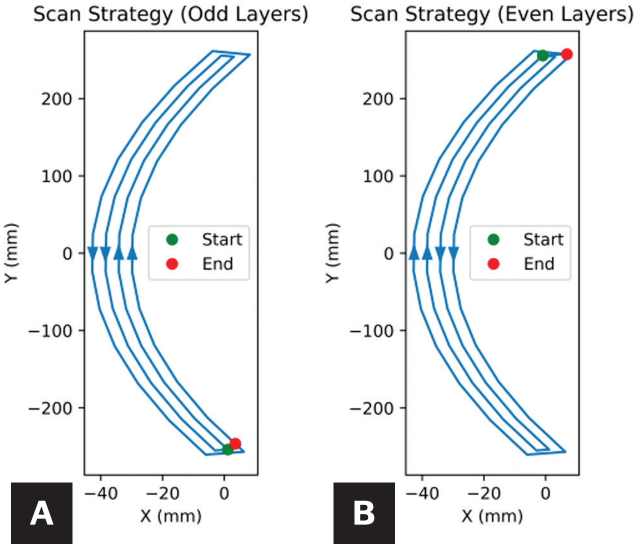

Fig. 5 — Tool path for: A — Odd layers; B — even layers. It consists of two passes, each with two inner beads and two outer beads.

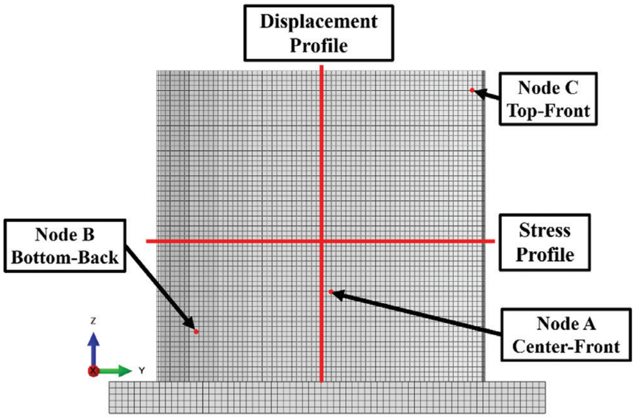

Fig. 6 — Identification of monitoring locations within the meshed volume of WAAM part for the extraction of temperature, displacement, and stresses as a function of time.

The deposition time per layer was around 2 min. The welding wires were changed three times during manufacturing (at layers 74, 160, and 213), resulting in a 10-min pause each time. Additionally, there were seven tip changes, each taking approximately 2 min, and a 3-min print stop, adding to 47 min of pauses (Ref. 35). As mentioned, these pauses that were not known prior to fabrication were included in the model. After manufacturing, the baseplate constraints were removed to evaluate the elastic spring-back, and a 3D laser scan was conducted to track part distortion.

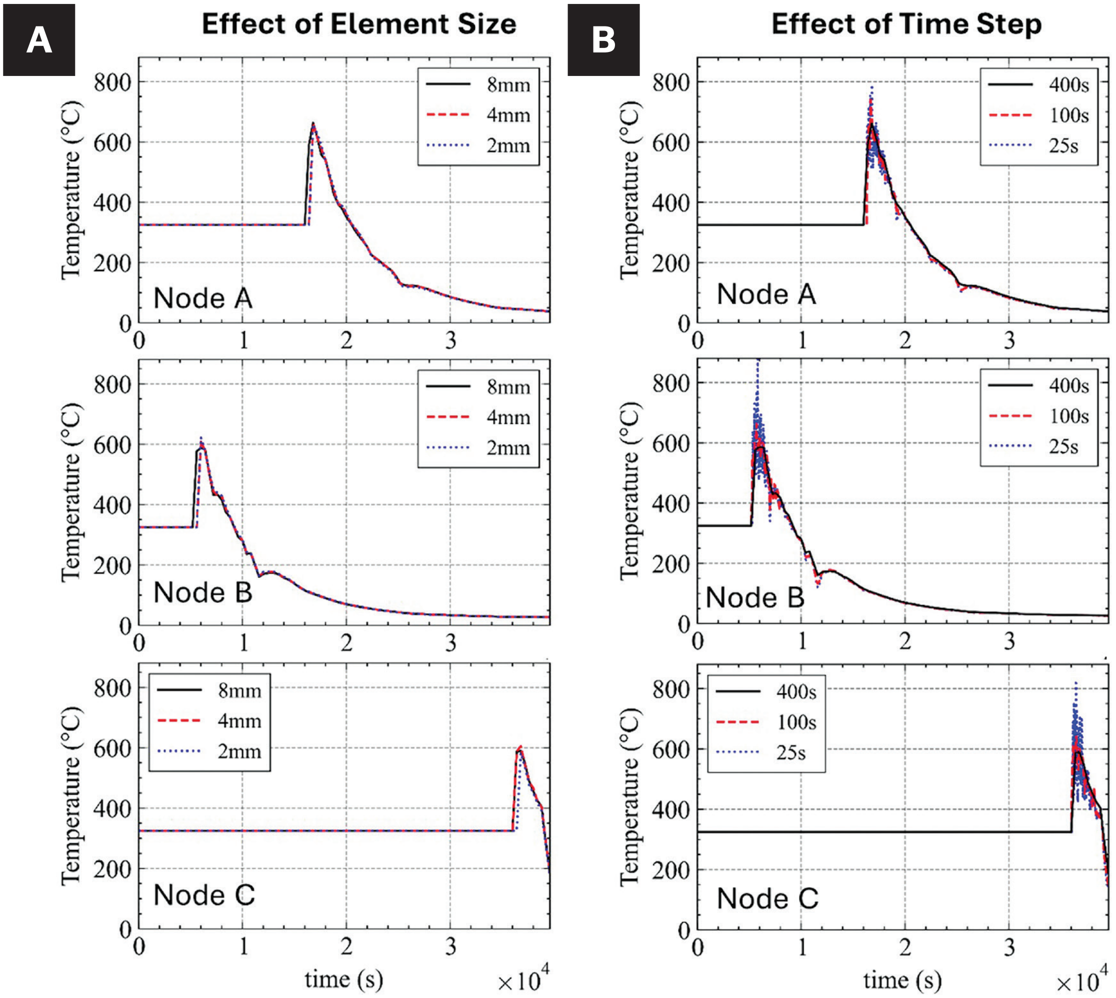

Fig. 7 — Effect of: A — Element size, l; B — time step size, Δt, on temperature profile at nodes A, B, and C. The time resolution with 8 mm element size shows a greater effect than element size on the predicted peak temperatures.

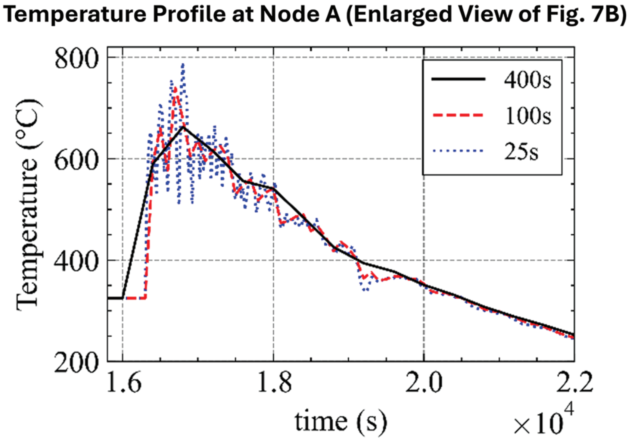

Fig. 8 — Enlarged view of temperature history from Node A. Oscillations in temperature were observed at a smaller time step of 100 s and 25 s due to the feature of multi-layer deposition AM. Also, a higher peak temperature was found at smaller time steps.

Role of Two Resolution Factors: Time and Element Size

The effects of two resolution factors — time increment and element size — were investigated. A decrease in time increment and element size correlated with increased temporal and spatial resolution, respectively. The time increment, denoted by Δt, specified the discrete interval of time over which time-dependent governing equations were being solved. It is known that a finer Δt in AM simulation results in a higher peak temperature than a coarse time step. First, moving the heat source in AM causes transient and localized temperature changes. With a finer Δt, the simulation could track the rapid movement of the heat source and transient heat transfer near the heat source more precisely, which allowed it to better capture the rapid thermal fluctuations and thermal gradient near the heat source as it passed by. In other words, a coarse Δt may not have captured the rapid temperature changes and thermal gradient precisely, leading to averaging of temperatures over coarse Δt, a more diffused temperature distribution, and, consequently, lower peak

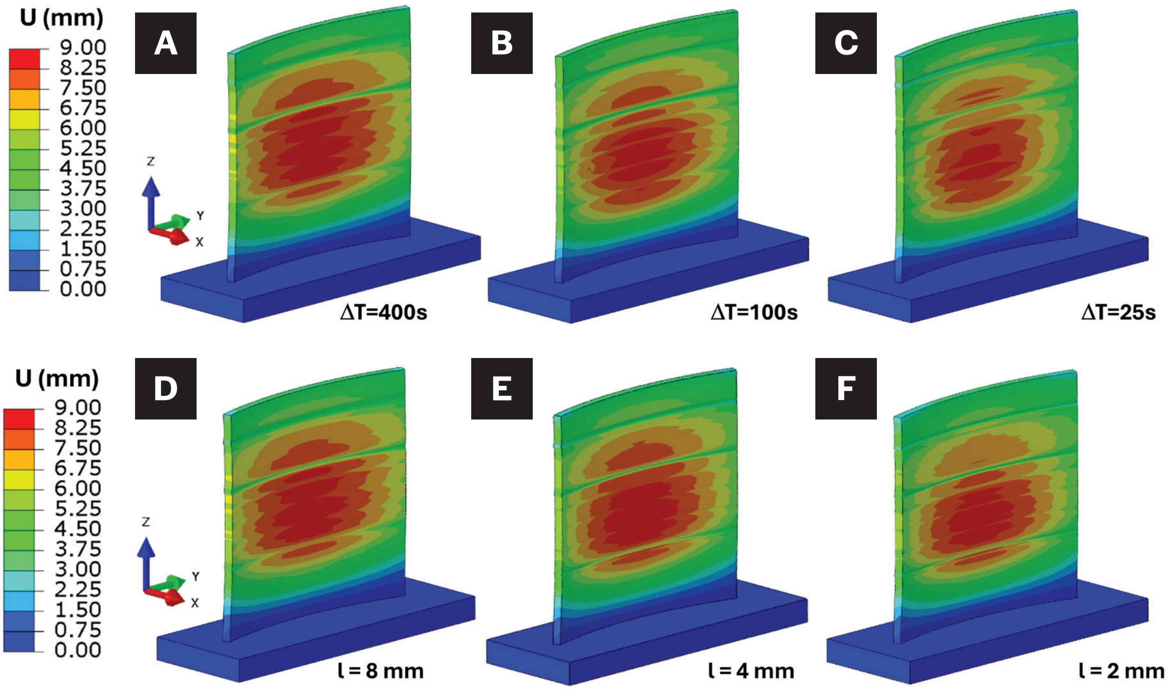

Fig. 9 — Predicted total displacement (i.e., distortion) showing the influence of time step: A — Δt = 400 s; B — Δt = 100 s; C — Δt = 25 s; the influence of element size: D — 8 mm; E — 4 mm; F — 2 mm.

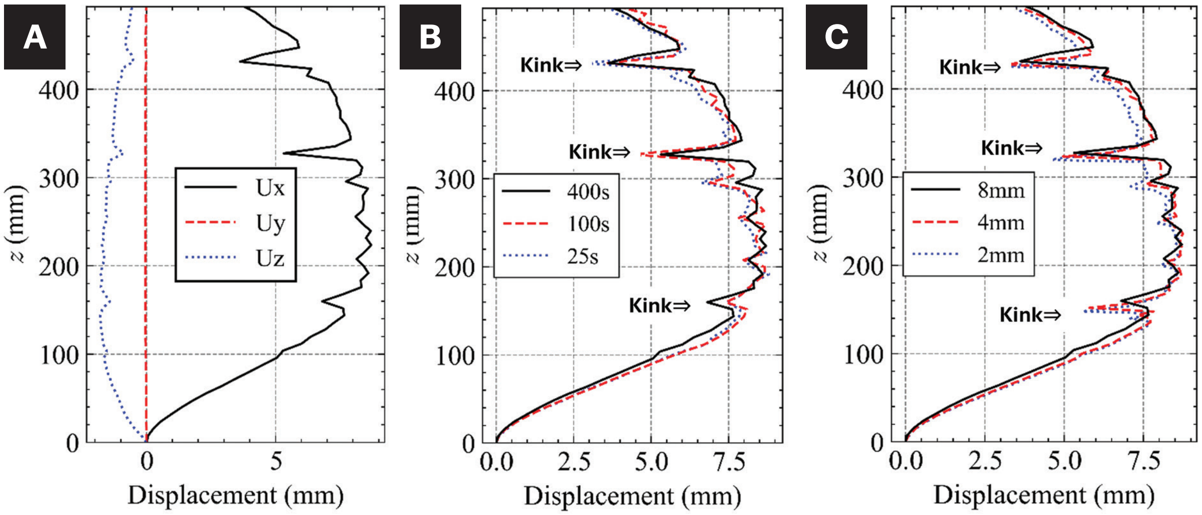

Fig. 10 — Vector components of total displacement: A — U_x, U_y, U_z along the z direction of the wall part in the 8 mm with Δ400 s analysis. The largest displacement is in the x direction. Effect of: B — time increment; C — element size on displacement in x direction along the centerline of the wall as shown in Fig. 6.

temperatures. Second, FEM with a finer Δt more accurately captured the maximum temperature at each position of the moving heat source, resulting in a more precise calculation of temperature rise. Conversely, the energy input from the heat source with a larger Δt was spread over a larger area/volume, leading to a lower peak temperature. Third, a smaller time step reduced numerical artifacts of discretization caused the heat to spread more widely. In other words, heat diffusion was more pronounced with a coarse Δt, resulting in a lower peak temperature. The other factor, element size (or length) l, influenced the number of points in the domain of an analysis. With a smaller element size, the simulation could capture the temperature more precisely, leading to accurate peak temperature prediction. Also, a finer element size reduced the heat diffusion effect. Lastly, it better represented geometric features and boundaries in regions with complex features. For each mesh, element length was approximately the same in all directions; therefore, element length, l, and element size were used interchangeably. Typically, when modeling welding and AM processes, element size in the build direction is equal to

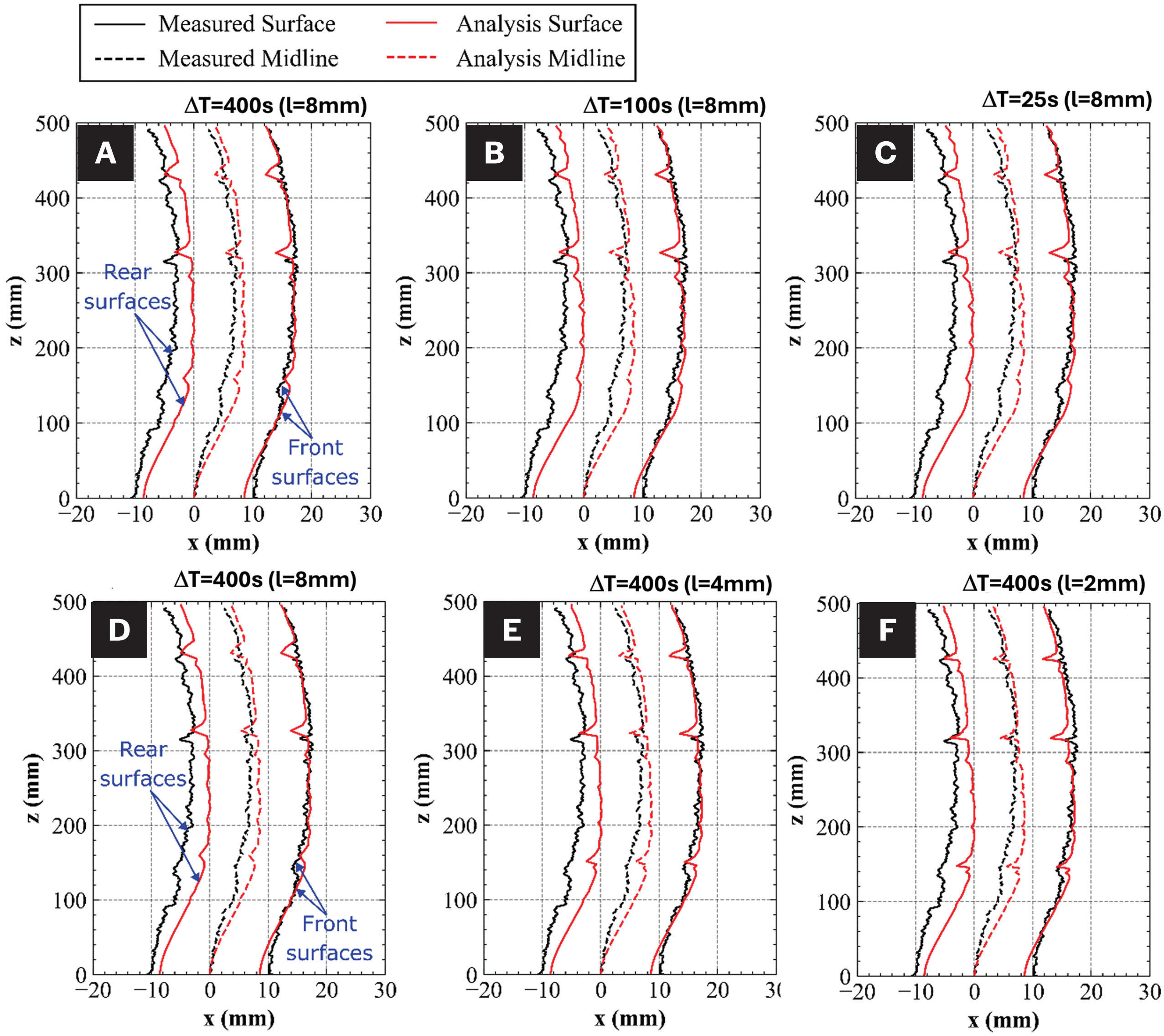

Fig. 11 — Calculated x-z midlines for: A — Δt = 400 s; B — Δt = 100 s; C — Δt = 25 s at 8 mm element size and for D — 8 mm; E — 4 mm; F — 2 mm element size at Δt = 400 s. The simulation effectively predicted the distortion behavior in the curved wall, with the distortion matching better on the front surface than on the rear surface.

or less than the deposition layer height to capture interlayer physics accurately. When modeling large parts, the number of layers is often in the hundreds. To keep computational costs down, coarser meshes with elements several times larger than the layer thickness are used(Refs. 39, 40,41). In our work, element sizes of 8 mm, 4 mm, and 2 mm, equivalent to 4, 2, and 1 layer (s) in the z direction, were first investigated with a 400 s time increment. The tool paths were modeled using the progressive element activation method. The size of the time step determined the extent of bead deposition. For instance, if the time step was longer than a layer time, all beads in a layer were activated. The time step of 25 s in the current work could resolve about six tracks. Element size and time increment were varied across five analyses, as listed in Table 1, with the 8 mm and 400 s analysis serving as the lowest resolution case for both time increment and element size output comparisons. Note that the element sizes listed for each simulation are the approximate global element size input into the mesh seeding parameters and vary depending on the dimensions of the part geometry. The approximate deposition cross-section was 8.6 mm wide × 2 mm high. To provide context, the Fourier (Fo) number for these conditions was also calculated with average thermal diffusivity at room temperature ($\alpha = 3.61956 \times 10^{-6}$ m^2/s) using the standard textbook equations ($F_o = \alpha \Delta t/(l^2)$). Ideally, the Fo should be less than 1 for non-steady transient heat transfer conditions. It is clear that none of our simulations, including most published research, can accurately predict thermal signatures. Our other attempts to reduce the spatial and temporal resolution beyond the values shown in Table 1 are beyond the scope of this paper.

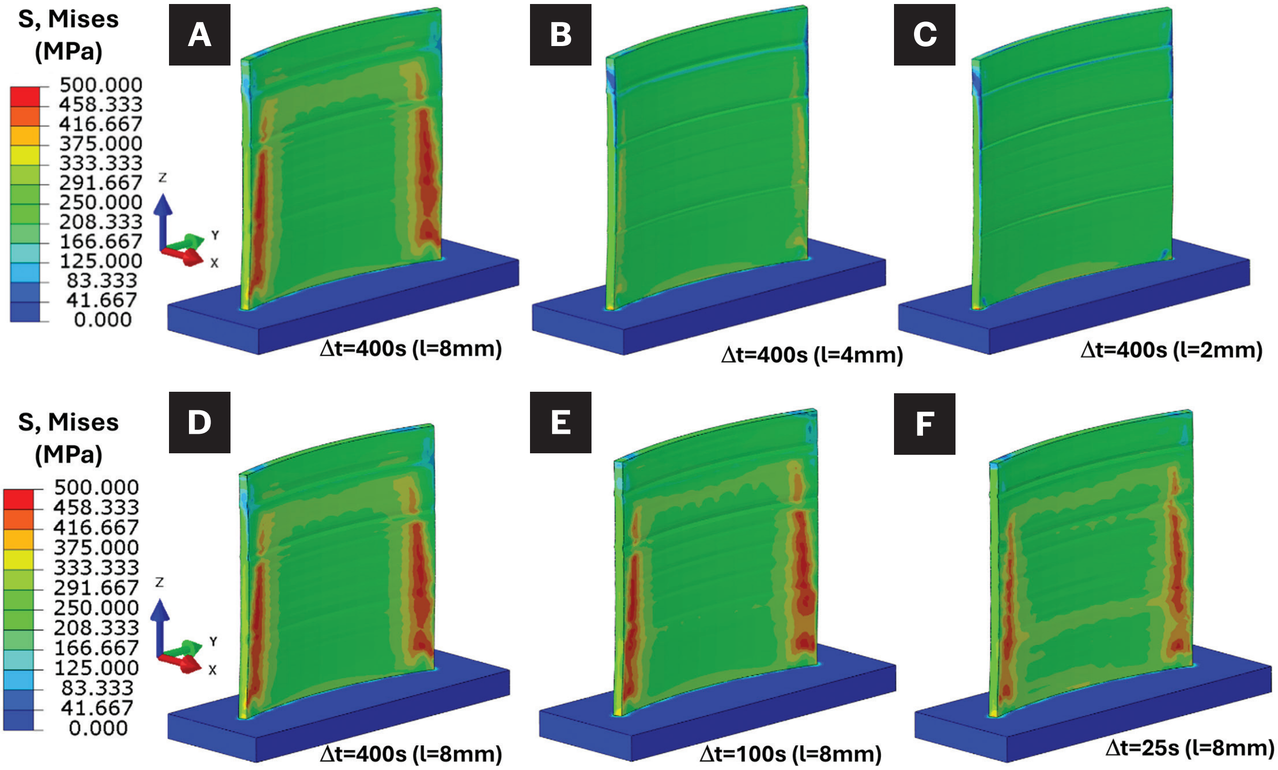

Fig. 12 — Predicted Residual von Mises stresses (MPa) across the curved wall face with the following element sizes: A — 8 mm; B — 4 mm; C — 2 mm vs. time resolution: D — Δt = 400 s; E — Δt = 100 s; and F — Δt = 25 s.

Table 3 — Mean Difference in Distortion Between Midlines Calculated From Prediction and Measurements

Increment Size	400 s	100 s	25 s
Mean Diff. (mm)	1.359	1.435	1.290
% Difference	—	5.5%	5.3%
Element Size	8 mm	4 mm	2 mm
Mean Diff. (mm)	1.359	1.425	1.253
% Difference	—	4.8%	8.4%

Results and Discussions

Standard Meshing Strategy

Figure 6 shows the monitoring locations of temperature, displacement, and stresses. The temperature profiles were taken from three A, B, and C node locations. The displacement and stress profiles were extracted from vertical and horizontal lines across the part face, denoted by red solid lines. The plotted locations were outlined to help other researchers to use the same approach for verification and validation of their own modeling schemes. These nodes were selected to get an overview of temperature signatures at different times during the WAAM process and to investigate temperature changes during deposition at the front face, back face, and at the center of the part. When selecting nodes to extract computational results, a node was selected on the 8 mm mesh, then the nearest node was used to get the closest node on the other meshes.

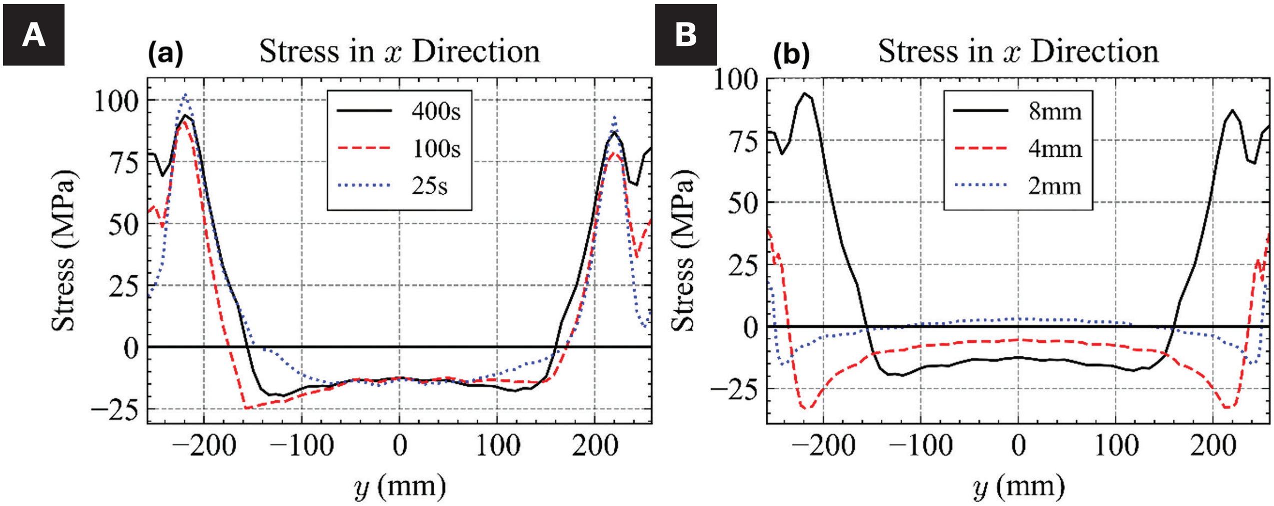

Fig. 13 — The stress component along the x-direction in the profile line for each increment in: A — Time resolution; B — element size.

Comparison of Temperature Profiles Across Two Resolution Factors

Figure 7 shows the temperature profile for nodes A, B, and C over time. In general, the temperature profiles from each monitoring location showed the same trend across different element sizes (8 mm, 4 mm, and 2 mm at 400 s) in Fig. 7A and different time step sizes (400 s, 100 s, and 25 s with 9 mm element size) in Fig. 7B. It was observed that the peak temperature increased with smaller time steps. At the same time, it remained similar even with an increase in element size. The peak temperature in Table 2 decreases as the time step increases, with values of 971.6°C, 784.5°C, and 698.4°C corresponding to time steps of 25 s, 100 s, and 400 s, respectively. The differences in peak temperature due to time step size are 273.2°C and 187.1°C compared to 400 s, representing 39.1% and 12.3% of the peak temperatures at 25 s and 100 s, respectively. In contrast, the differences in peak temperature due to changes in element size are 15.1°C between 8 mm and 4 mm and 15.6°C between 8 mm and 2 mm. These changes represent deviations of approximately 2.2% and 2.3% compared to the 8 mm case and can be considered negligible. The results show that time resolution had a greater effect than element size on the predicted peak temperatures. Note that the temperature at Node C did not fully cool down to RT (remaining around 200°C). Further cooling to RT can lead to additional distortion relaxation in the upper region above 300 mm after the first kink in Fig.10.

Temperature fluctuations between layers were not captured by the larger 400 s time step. However, as the time step decreased to 100 s and 25s, these fluctuations were more precisely resolved, as shown in Fig. 8. This indicates that time resolution had a stronger impact on the results in thermal analysis. In the absence of temperature data during the part's deposition, it can be assumed that the 25 s analysis generated maximum temperatures closest to typical deposited temperatures while still under-predicting the real peak temperature.

Comparison of Displacement Across Two Resolution Factors

The variations in magnitude of total displacement, *U*, at different time step sizes of 400 s, 100 s, and 25 s and element sizes of 8 mm, 4 mm, and 2 mm are shown in Fig. 9. Regardless of time step and element sizes, the highest distortion was found at the center section of the curved wall and radiated outward toward the edges. The difference in the maximum displacement across all analyses was 0.124 mm. The curved wall geometry was symmetric only with respect to the y and x-z planes, not the y-z plane. Since the inner radius was shorter than the outer radius, an inward bending moment was generated during cooling. Additionally, the curved wall underwent shrinkage displacement along the z-direction, inducing a downward bending tendency. Notably, the bottom region of the part was fixed to the substrate, which resulted in higher stiffness and required a greater mechanical driving force to bend near the bottom region. Combined, the inward and downward bending moments possibly caused the part to bend forward during cooling and backward during heating with different magnitudes in the bottom and upper regions (Ref. 35).

Breaking *U* into its vector components U_x, U_y, U_z along the height of the part, as shown in Fig. 10A, revealed that the largest component was in the *x* direction, where the face was shifting in the *x*+ direction. In the *x* direction, there was a difference of 0.096 mm in the maximum displacement values across all analyses. This can be seen in Figs. 10B and C, which plot U_x for each simulation. There was a noticeable local minimum in displacement at the z height of each wire change in Figs. 10B and C, which was accompanied by a printing pause. The three low-displacement regions due to a longer interlayer time from the 10-minute wire changing can be seen in Figs. 10B and C, marked as "kink". These regions are not at the same z height as the mesh size changes, with the largest difference in z height between the local minimums being approximately 12 mm.

Table 4 — Total Solver Time Across Mesh Sizes

Element Size	8 mm	4 mm	2 mm	2 mm X	2 mm Z
Total Solve Time (h)	0.33	2.35	49.97	9.32	4.36

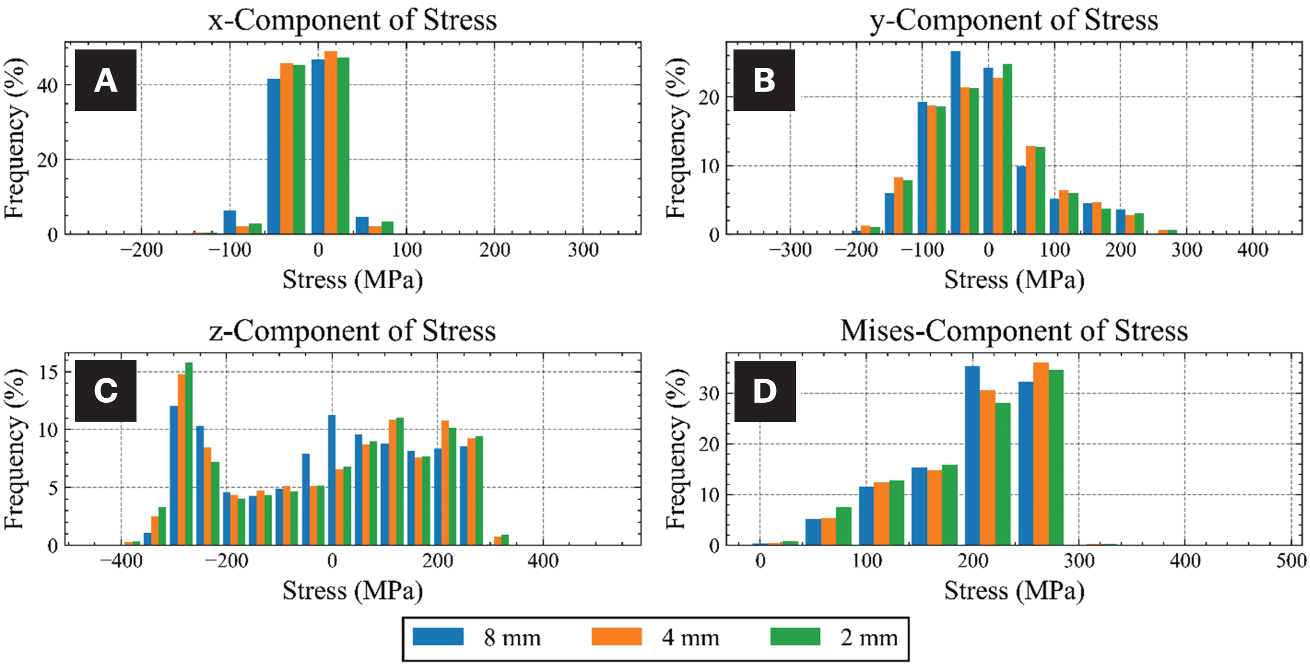

Fig. 14 — Distribution of the magnitude of the stress components at integration points across element sizes. Stresses in the z-direction had the largest range of stress distribution with a noticeable compressive peak.

This is attributed to the "lumping" of layers that occur with a larger element size.

Comparison of Prediction with Measurements

Due to the large surface irregularities of the WAAM process, the midlines of the front and back surfaces of the wall were calculated by averaging the two-surface data in Fig. 11. At an XZ plane aligned with the center of the part, the front and back surfaces were analyzed using point cloud data from the manufactured part. The deformed profiles were created by adding displacement data to the initial positional data of each node. Using the midpoint formula, a line at the center of the part was generated for comparison. Following the calculation, the analyses' midlines were linearly interpolated to the same number of points as the measured data for comparison. Comparing the predicted to the measured data reveals that while both FEA and the actual part form kink deformations (locally negative) at the layers where the wire was changed, as shown in Fig. 11, the FEA possibly overpredicted the magnitude of distortion at layers 74, 160, and 213. This is attributed to the machine seeking a restart location after the pauses on the deformed part and dynamically correcting some of the pause-induced deformation. Additionally, the locations of these deformations did not precisely match the measured kinks in the z-direction in the FEA due to the low spatial resolution (i.e., larger element size) with the 2 mm element size providing the closest agreement and the smallest difference. The plotted midlines (see Fig. 11) show a greater divergence of the analyses from the dataset in the lower half ($z < 250$ mm) than in the upper half ($z > 250$mm). The maximum errors between analyses and measurements were in this lower region.

The highest resolution models in increment and mesh size (25 s and 2 mm) had the lowest calculated absolute mean differences relative to the measured surfaces in Table 3. The relative percentage difference was 4.8% between 8 mm and 4 mm and 8.4% between 8 mm and 2 mm. Similarly, the relative percentage difference was 5.5% between 400 s and 100 s and 5.3% between 400 s and 25 s. The overall range of mean differences across analyses was 0.172 mm. Given the part dimensions of approximately 500 mm, this range is considered relatively minor.

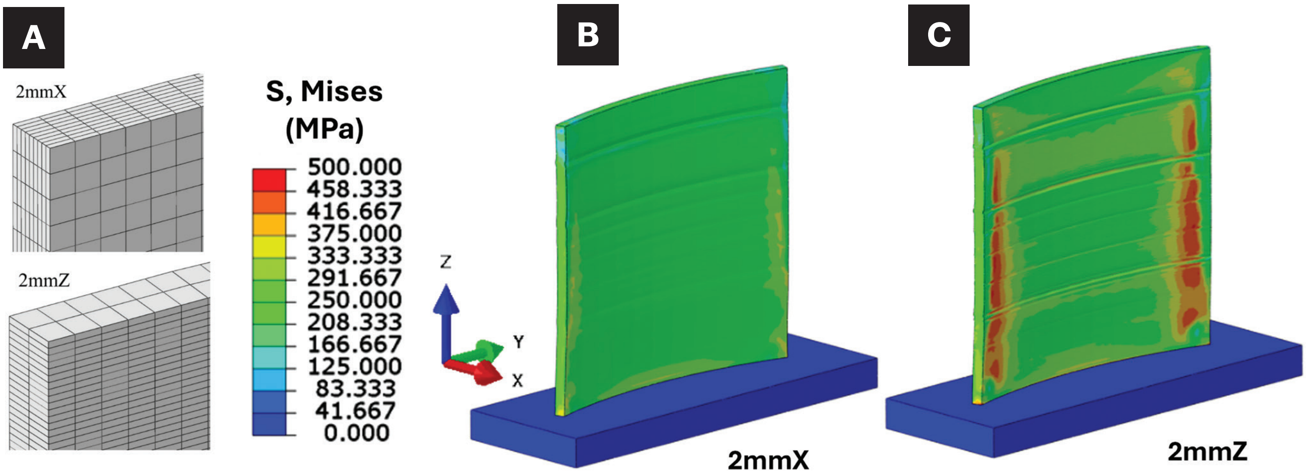

Fig. 15 — Predicted residual von Mises stresses (MPa) across the curved wall face for different mesh strategies: A — Schematic illustration of the directional meshing strategy, which in turn modifies the constraints with respect to the motion of the heat source, biased meshes of B — 2 mmX; C — 2 mmZ.

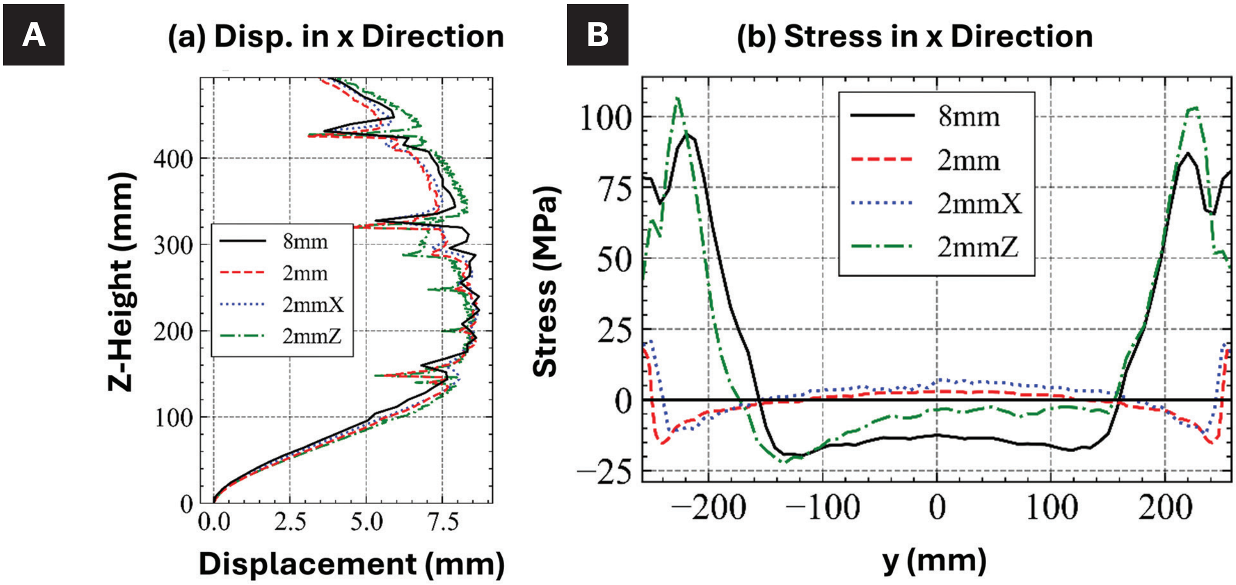

Fig. 16 — Comparison of predicted results from directionally biased meshing to standard meshing strategy: A — Displacement; B — von Mises stress in x direction for the 2 mm, 8mm, and mesh sizes.

Predicted Residual Stress Distributions

Comparisons of von Mises stress distributions at different time step sizes of (a) 400 s, (b) 100 s, and (c) 25 s and element sizes of (d) 8 mm, (e) 4 mm, and (f) 2 mm are shown in Fig. 12. The comparison shows a noticeable effect of spatial resolution (i.e., element size) on residual stress distributions in Figs.12A–C, while the time increment had a minor impact on the stress distribution in Figs. 12D–F. High-stress regions were observed on both sides of the wall front in Fig. 12A and 12D–F, forming two vertical, columnar-like bands. High stresses were observed near the side edges, creating columnar stress patterns along the z-direction, while weaker stresses occurred near the central region in Figs. 12A and 12D–F. The deposited heat flowed toward the part center and down to the cooler substrate along the build direction. Consequently, it led to the largest shrinkage toward the center-build direction, resulting in a depression at the top-center and on each vertical side. This pattern was observed in neutron diffraction measurement (Ref. 32). In curved walls, the forward bending moment increases the stress levels in the x-direction. With smaller element sizes of 4 mm and 2 mm in Figs. 12B and C, the high-stress regions disappeared from the sides. The time increment had an impact on the width of these regions in Figs. 12D–F; however, they still had maximum von Mises stresses on the sides of the wall front.

Figure 13 shows x-component stress variations, σ_{xx}, along the horizontal line shown in Fig. 6. The stress distributions at

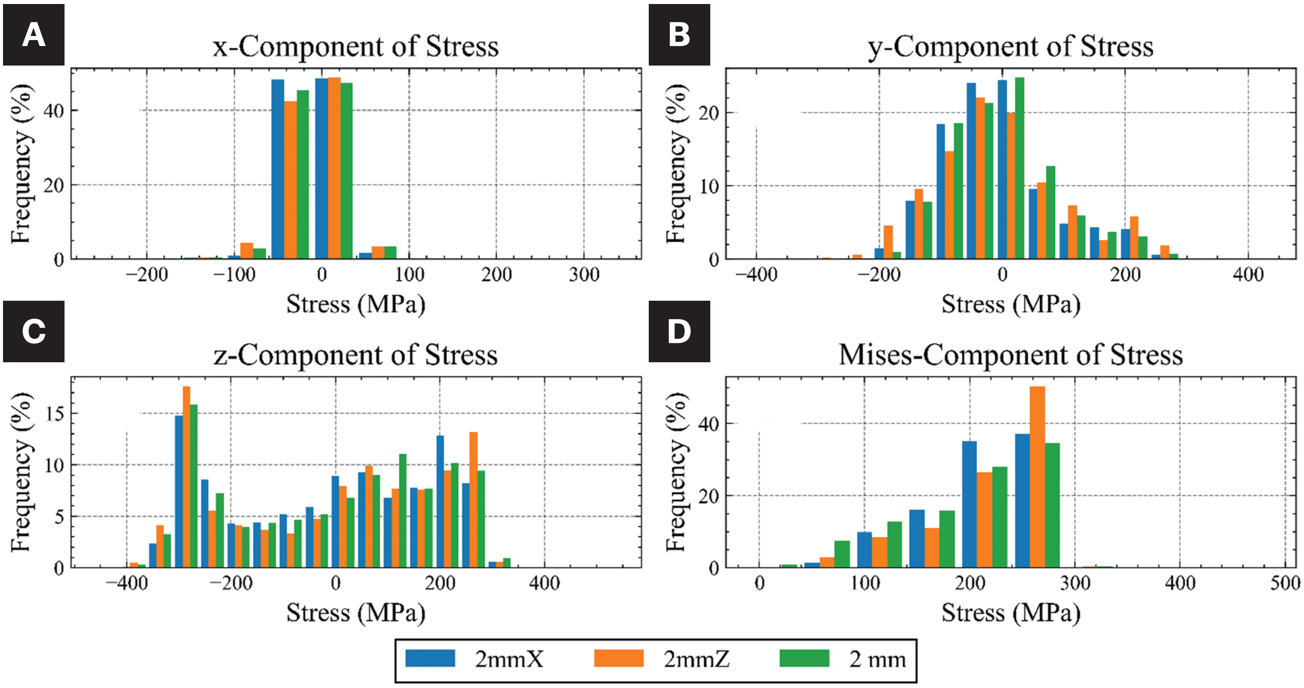

Fig. 17 — Predicted magnitude of stress components at integration points across hybrid and 2 mm meshes.

the three time increments with an 8 mm element size in Fig. 13A are analogous, showing high-tensile stresses at the sides and compressive stresses in the center region of the wall. The stresses across the time increments converge most closely at the center, with the greatest differences observed at the edges of the wall. In Fig. 13B, the larger element size of 8 mm shows higher tensile stresses around 85 MPa compared to 25 MPa for the 4 mm and 2 mm element sizes. Without measured data for the residual stresses, it is assumed that the highest-resolution mesh, 2 mm, generated the most reliable stress state. The peaks observed with the 8 mm element size might have been inaccuracies resulting from the low mesh resolution.

For further statistical analysis, the stress values of each directional component (x, y, and z) were extracted from all elements across the wall at each integration point. The values are plotted in histograms in Fig. 14 using a bin size of 50 MPa. Although the overall trends in stress distributions are fairly similar, observable differences are found in each directional component. The x-component stresses in Fig. 14A range from −100 MPa to +100 MPa, showing the lowest magnitude of stress distribution compared to the y-component (−200 MPa to +300 MPa) in Fig. 14B and the z-component (−400 MPa to +350 MPa) in Fig. 14C. The y-component of stresses in Fig. 14B trends toward more tensile in the finer meshes, while the 8 mm size shows stronger compressive stresses in comparison. Stresses in the z-direction had the largest range of stress distribution with a noticeable compressive peak in the range of -100 MPa to 0 MPa, which may be numerical inaccuracies caused by the large element size.

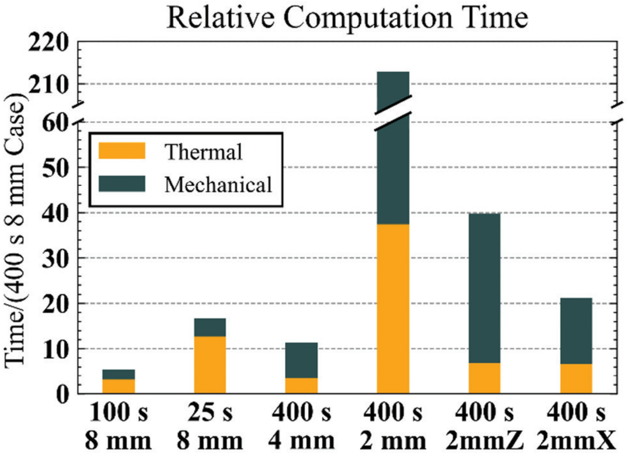

Fig. 18 — Comparison of wall-clock solution times relative to simulation #1 (400 s and 8 mm).

Directional Meshing Scheme

Since the predicted residual stress distribution showed sensitivity to mesh size (i.e., different constraints on the meshes leading to different gradients of plastic strain gradients), we investigated the impact of element geometry. Two additional meshes with directionally higher resolutions were created in Fig. 15A. Each approach used biased meshes with an element length of 8 mm in two directions and 2 mm in the third. Mesh "2 mmX" was 2 mm in the wall thickness direction, while "2 mmZ" had a higher resolution in the build height direction. The 2 mmZ meshing strategy generated a mesh closer to some approaches seen in the literature, which respects the layer-wise deposition of the AM process by using an element height equal to the layer height. Since the 8 mm mesh consisted of only two elements in through-thickness, the 2 mmX strategy was deployed to improve the transversal resolution of the model, because the σ_{xx} showed the greatest discrepancy in distribution and magnitude with respect to element size in the previous experiment. Models for each of the new meshes used a 400 s time increment. Figure 15B and C shows the von Mises stress distribution across the curved wall comparing biased mesh sizes of 2 mm in the x-direction, 2 mmX, and 2 mm in the z-direction, 2mmZ. Interestingly, the 2 mmX mesh resembles the initial case with a 2 mm element size, while the 2 mmZ mesh shows a stress distribution similar to the 8 mm element size.

Figure 16 shows the distribution of displacement and stress in the x direction along the build direction. Looking at the displacements, as expected, the distortion behavior was similar regardless of element sizes and types. However, the 2 mmZ mesh, shown in green, showed a larger deviation in displacement toward the top of the part compared to the others, as shown in Fig. 16A. The stress distributions shown in Fig. 16B support that the 2 mmX mesh, shown in blue, produced a stress distribution closer to that of the initial 2 mm element size mesh. Similar to the previous analysis shown in Fig. 14, the distribution of stress components is shown in Fig. 17.

Computational Costs

Total solver times for the 2 mmX and 2 mmZ meshes are compared in Table 4; the 2 mmX case was able to generate similar stress results to the highest spatial resolution case with a 91.3% reduction in solver time in Fig. 18. Decreasing the element size from 8 mm to 2 mm resulted in a ~49.6 h increase in solver time, while decreasing the time increment from 400 s to 25 s resulted in a ~0.8-h increase. The solver time behaved as expected; adding more increments to solve is less computationally expensive than increasing the time to solve per increment.

Figure 18 shows the solution times with a common reference frame by normalizing each model's thermal and mechanical computation time by the baseline 400-s, 8 mm case. Decreasing increment size had a larger influence on thermal solution time than mechanical solution time; for the 25 s case, the thermal analysis took 12.7× longer to solve, while the mechanical analysis took 4× longer to reach a solution. This is because the smaller increment sizes had sharper thermal gradients with higher maximum temperatures, thus needing to accommodate a larger range of temperature-dependent properties for a given increment. Regarding the hybrid meshing scheme, the 2 mmX model was 21.2× slower than the initial model, while the 2 mm model was 212.8× slower. The difference in mechanical solution times between the two biased meshing approaches (2 mmZ and 2 mmX) can be attributed to the 2 mmZ analysis, which involves more complex element activation for each layer along with a more number of reheating events.

Implications of the Current Research

In general, the size of the time increment and element significantly influences both the quality of the simulation and the overall computation time. A large element size may fail to capture changes of thermal and mechanical behavior in local areas. A large time step size may miss important details in peak temperature and thermal gradients near the heat source. Both time increment and element size were varied with relatively low impact on the predicted distortion. When deploying FEA to understand the relationship between geometry and bulk distortion behavior in a part, lower resolution models can offer a pathway to rapid prediction and design iterations due to the extreme computational speed. An increase in element size came with a large reduction in computational cost. This approach could also be used to get an approximation of whether the maximum distortion of a geometry will be within a provided tolerance. The caveat that must be considered is that a decrease in mesh and increment fidelity will not necessarily provide a physically accurate look into the thermal history and residual stress development from the WAAM process. An additional avenue to explore is the implementation of the same investigation on larger geometries with higher degrees of complexity. For further verification and validation, it is important to investigate whether biased meshes yield similar results on non-wall geometries. By evaluating the impact of model resolution across various geometries in large-scale WAAM parts, best practices in meshing and time incrementation can be established for efficiently predicting displacement and residual stresses. A final note is that these findings are not specific to the software used in this research and will be similar in all finite element methodologies. To arrive at best practices, the AM community must perform V&V across different classes of geometries to arrive at consistent residual stress and distortion measurements with pragmatic mesh size and time resolution. Further experimentation, such as neutron diffraction, must be conducted to measure residual stress distribution and phase transformation across the whole sample with voxel-by-voxel resolution (Ref. 42) across simple to complex WAAM geometries, similar to the work performed on L-PBF and E-PBF samples (Ref. 43). Furthermore, we recommend round-robin modeling and measurement of both residual stress and distribution in WAAM samples with controlled geometries, scan paths, and process parameters to improve consistency. Such evaluations have been performed before for the modeling of welds (Ref. 44).

Conclusions

The effect of time increment and element size on the calculation of distortion and residual stresses has been investigated on a part-scale curved-wall with dimensions of approximately 500 mm tall × 500 mm wide. The results provide a pathway to perform verification and validation of computational models for optimization of large-scale WAAM parts. The calculations showed that the time increment had a greater impact on the thermal history than the element size. In contrast, the element size significantly affected the residual stress distribution with a smaller effect on distortion. Across all cases, nodal displacement yielded consistent results; similar patterns of displacement were present across the models, and the largest difference between predicted maximum displacement in any direction was less than 0.2 mm. In contrast, element size had a greater impact on residual stress distributions, resulting in regions of higher residual stress across the sides of the wall front. The high-stress regions forming two vertical, columnar-like bands were found only at a large element size of 8 mm, not at 4 mm and 2 mm; as the element size was decreased, the maximum value decreased and shifted toward the edge of the part. The differences in the distribution of stress results between 8 mm, 4 mm, and 2 mm could be attributed to the very low spatial resolution perpendicular to the tool path. The directionally biased meshes confirmed the influence of the spatial resolution in different directions (i.e., perpendicular to the tool path and build direction). The results showed that a finer mesh size perpendicular to the tool path improves the prediction of residual stress, closely matching the high-resolution cases with 2 mm elements in all directions. In conclusion, increasing both the time increment and element size has relatively little impact on distortion prediction. When using FEA to understand the relationship between geometry and overall distortion behavior, lower-resolution models offer a practical pathway for rapid prediction or for analyzing meter-scale, large-part deformation due to substantial computational time savings.

Acknowledgments

This manuscript has been authored by UT-Battelle, LLC under Contract No. DE-AC05-00OR22725 with the U.S. Department of Energy. The United States Government retains, and the publisher, by accepting the article for publication, acknowledges that the United States Government retains a non-exclusive, paid-up, irrevocable, worldwide license to publish or reproduce the published form of this manuscript, or allow others to do so, for United States Government purposes. The Department of Energy will provide public access to these federally sponsored research results per the DOE Public Access Plan (*energy.gov/downloads/doe-public-access-plan*).

This research at UTK was supported by the Department of the Navy, Office of Naval Research under ONR award number N00014-18-1-2794. Any opinions, findings, conclusions, or recommendations expressed in this material are those of the author(s) and do not necessarily reflect the views of the Office of Naval Research. Part of this research was supported by the U.S. Department of Energy, Office of Energy Efficiency and Renewable Energy, Advanced Materials and Manufacturing Technologies Office (AMMTO) under contract number DE-AC05–00OR22725.

References

1. U.S. Department of Energy. 2022. Domestic casting industry. Dawnbraker Inc. Retrieved from *science.osti.gov/-/media/sbir/pdf/Market-Research/AMO---Metal-Casting-August-2022-Public.pdf.*

2. U.S. Department of Defense. 2022. Securing defense-critical supply chains. Retrieved from *media.defense.gov/2022/feb/24/2002944158/-1/-1/1/dod-eo-14017-report-securing-defense-critical-supply-chains.pdf.*

3. Williams, S. W., Martina, F., Addison, A. C., Ding, J., Pardal, G., and Colegrove, P. 2016. Wire + arc additive manufacturing. *Materials Science and Technology* 32(7): 641–647.

4. Hassen, A. A., Noakes, M., Nandwana, P., Kim, S., Kunc, V., Vaidya, U., Love, L., and Nycz, A. 2020. Scaling up metal additive manufacturing process to fabricate molds for composite manufacturing. *Additive Manufacturing* 32: 101093.

5. Dias, M., Pragana, J. P., Ferreira, B., Ribeiro, I., and Silva, C. M. 2022. Economic and environmental potential of wire-arc additive manufacturing. *Sustainability* 14(9): 5197.

6. Kokare, S., Oliveira, J. P., and Godina, R. 2024. Exploring the environmental and economic benefits of wire arc additive manufacturing compared to subtractive manufacturing. *Procedia CIRP* 130: 3–8.

7. Evjemo, L. D., Langelandsvik, G., and Gravdahl, J. T. 2019. Wire arc additive manufacturing by robot manipulator: Towards creating complex geometries. *IFAC-PapersOnLine* 52(11): 103–109.

8. Arbogast, A., Nycz, A., Noakes, M. W., Wang, P., Masuo, C., Vaughan, J., Love, L., Lind, R., Carter, W., and Meyer, L. 2024. Strategies for a scalable multi-robot large-scale wire arc additive manufacturing system. *Additive Manufacturing Letters* 8: 100183.

9. Ding, D., Pan, Z., Cuiuri, D., and Li, H. 2015. Wire-feed additive manufacturing of metal components: Technologies, developments and future interests. *International Journal of Advanced Manufacturing Technology* 81: 465–481.

10. Derekar, K. 2018. A review of wire arc additive manufacturing and advances in wire arc additive manufacturing of aluminium. *Materials Science and Technology* 34(8): 895–916.

11. Thompson, M. K., Moroni, G., Vaneker, T., Fadel, G., Campbell, R. I., Gibson, I., Bernard, A., Schulz, J., Graf, P., and Ahuja, B. 2016. Design for additive manufacturing: Trends, opportunities, considerations, and constraints. *CIRP Annals* 65(2): 737–760.

12. Jafari, D., Vaneker, T. H., and Gibson, I. 2021. Wire and arc additive manufacturing: Opportunities and challenges to control the quality and accuracy of manufactured parts. *Materials & Design* 202: 109471.

13. Wu, B., Pan, Z., Ding, D., Cuiuri, D., Li, H., Xu, J., and Norrish, J. 2018. A review of the wire arc additive manufacturing of metals: Properties, defects and quality improvement. *Journal of Manufacturing Processes* 35: 127–139.

14. Plotkowski, A., Saleeby, K., Fancher, C. M., Haley, J., Madireddy, G., An, K., Kannan, R., Feldhausen, T., Lee, Y., and Yu, D. 2023. Operando neutron diffraction reveals mechanisms for controlled strain evolution in 3D printing. *Nature Communications* 14(1): 4950.

15. Cunningham, C., Flynn, J. M., Shokrani, A., Dhokia, V., and Newman, S. T. 2018. Strategies and processes for high quality wire arc additive manufacturing. *Additive Manufacturing* 22: 672–686.

16. Turgut, B., Gürol, U., and Onler, R. 2023. Effect of interlayer dwell time on output quality in wire arc additive manufacturing of low carbon low alloy steel components. *International Journal of Advanced Manufacturing Technology* 126(11): 5277–5288.

17. Masubuchi, K. 1980. *Analysis of welded structures: Residual stresses, distortion, and their consequences*. Oxford and New York: Pergamon Press.

18. Goldak, J. A., and Akhlaghi, M. 2005. *Computational welding mechanics*. Springer Science & Business Media.

19. Huang, H., Ma, N., Chen, J., Feng, Z., and Murakawa, H. 2020. Toward large-scale simulation of residual stress and distortion in wire and arc additive manufacturing. *Additive Manufacturing* 34: 101248.

20. Denlinger, E. R., Irwin, J., and Michaleris, P. 2014. Thermomechanical modeling of additive manufacturing large parts. *Journal of Manufacturing Science and Engineering* 136(6): 061007.

21. Zhao, X. F., Wimmer, A., and Zaeh, M. F. 2023. Experimental and simulative investigation of welding sequences on thermally induced distortions in wire arc additive manufacturing. *Rapid Prototyping Journal* 29(11): 53–63.

22. Ali, M. H., and Han, Y. S. 2023. A finite element analysis on the effect of scanning pattern and energy on residual stress and deformation in wire arc additive manufacturing of EH36 steel. *Materials* 16(13).

23. Israr, R., Buhl, J., Elze, L., and Bambach, M. 2018. Simulation of different path strategies for wire-arc additive manufacturing with Lagrangian finite element methods. *LS-DYNA Forum*.

24. Tsai, C., and Kim, D. 2005. "Understanding residual stress and distortion in welds: An overview." In *Processes and mechanisms of welding residual stress and distortion* , edited by Feng, Z., 3–31. Cambridge: Woodhead Publishing Limited.

25. Ahmad, S. N., Manurung, Y. H., Adenan, M. S., Yusof, F., Mat, M. F., Prajadhiana, K. P., Minggu, Z., Leitner, M., and Saidin, S. 2022. Experimental validation of numerical simulation on deformation behaviour induced by wire arc additive manufacturing with feedstock SS316L on substrate S235. *International Journal of Advanced Manufacturing Technology* 119: 1951–1964.

26. Pont, D., and Guichard, T. 1995. Sysweld®: Welding and heat treatment modelling tools. *Computational Mechanics '95: Theory and Applications* 248–253.

27. Babu, S. S. 2010. "Introduction to integrated weld modeling. Metals process simulation." In *Metals Process Simulation*, 411–431.

28. American Welding Society. 2012. AWS A9.5:2013, *Guide for verification and validation in computational weld mechanics*. 1st Edition.

29. Yang, Y., Zhou, X., and Li, Q. 2021. A computationally efficient thermo-mechanical model for wire arc additive manufacturing. *Additive Manufacturing* 46.

30. Cattenone, A., Morganti, S., Alaimo, G., and Auricchio, F. 2019. Finite element analysis of additive manufacturing based on fused deposition modeling: Distortions prediction and comparison with experimental data. *Journal of Manufacturing Science and Engineering* 141.

31. Lu, X., Lin, X., Chiumenti, M., Cervera, M., Hu, Y., Ji, X., Ma, L., Yang, H., and Huang, W. 2019. Residual stress and distortion of rectangular and S-shaped Ti-6Al-4V parts by directed energy deposition: Modelling and experimental calibration. *Additive Manufacturing* 26: 166–179.

32. Nycz, A., Lee, Y., Noakes, M., Ankit, D., Masuo, C., Simunovic, S., Bunn, J., Love, L., Oancea, V., Payzant, A., and Fancher, C. M. 2021. Effective residual stress prediction validated with neutron diffraction method for metal large-scale additive manufacturing. *Materials & Design* 205.

33. Deering, R. A. 2018. Additive manufacturing part level distortion sensitivity analysis within Abaqus on a thin-walled, tubular structure.

34. Prajadhiana, K. P., Manurung, Y. H., Fateri, M., Choo, H. L., Rahaman, W. E. W. A., Adenan, M. S., Ambarita, H., Busari, Y. O., Ishak, D. P., and Taufek, T. 2025. Distortion analysis of WAAM component using thermo-mechanical, inherent strain and experimental methods. *Progress in Additive Manufacturing* 10(10): 1–17.

35. Lee, Y., Nycz, A., Simunovic, S., Meyer, L., Vaughan, D., Carter, W., Babu, S. S., Vaughan, J., and Love, L. 2023. Prediction and understanding of non-linear distortion on large curved wall manufactured by wire-arc direct energy deposition. *Additive Manufacturing Letters* 7: 100173.

36. Goldak, J., Chakravarti, A., and Bibby, M. 1984. A new finite element model for welding heat sources. *Metallurgical Transactions B* 15: 299–305.

37. Outinen, J., and Mäkeläinen, P. 2004. Mechanical properties of structural steel at elevated temperatures and after cooling down. *Fire and Materials* 28: 237–251.

38. Özcan, A., Kollmannsberger, S., Jomo, J., and Rank, E. 2019. Residual stresses in metal deposition modeling: Discretizations of higher order. *Computers and Mathematics with Applications* 78: 2247–2266.

39. Dassault Systèmes. 2022. Thermomechanical simulation of additive manufacturing processes.

40. Liang, X., Hayduke, D., and To, A. C. 2021. An enhanced layer lumping method for accelerating simulation of metal components produced by laser powder bed fusion. *Additive Manufacturing* 39: 101881.

41. Malmelöv, A., Lundbäck, A., and Lindgren, L.-E. 2019. History reduction by lumping for time-efficient simulation of additive manufacturing. *Metals* 10(1): 58.

42. Lee, Y., Nandwana, P., Gibson, B., Mhatre, P., Rojas, J. O., Prabhune, B., Thornton, A., Vaughan, J., and Simunovic, S. 2024. Integrated top-down process and voxel-based microstructure modeling for Ti-6Al-4V in laser wire direct energy deposition process. *Materials & Design* 247: 113434.

43. Sochalski-Kolbus, L. M., Payzant, E. A., Cornwell, P. A., Watkins, T. R., Babu, S. S., Dehoff, R. R., Lorenz, M., Ovchinnikova, O., and Duty, C. 2015. Comparison of residual stresses in Inconel 718 simple parts made by electron beam melting and direct laser metal sintering. *Metallurgical and Materials Transactions A* 46: 1419–1432.

44. Truman, C. E., and Smith, M. C. 2009. The NeT residual stress measurement and modelling round robin on a single weld bead-on-plate specimen. *International Journal of Pressure Vessels and Piping* 86: 1–2.

BRANDON SOLSBEE and **SUDARSANAM SURESH BABU** are with the Department of Mechanical, Aerospace, and Biomedical Engineering, University of Tennessee, Knoxville, Tenn. **YOUSUB LEE** (*leey@ornl.gov*) and **SRDJAN SIMUNOVIC** are with the Computational Sciences and Engineering Division, Oak Ridge National Laboratory, Oak Ridge, Tenn. **BABU** is also with the Manufacturing Sciences Division, Oak Ridge National Laboratory, Oak Ridge, Tenn., and the Department of Materials Science and Engineering, University of Maryland, College Park, Md.